Self-induced flow and heat transfer in a rotating tube

S. Gilham
W. S. Atkins Science & Technology, Epsom, Surrey, UK

P. C. Ivey
School of Mechanical Engineering, Cranfield Institute of Technology, Cranfield, Beds, UK

J. M. Owen
School of Mechanical Engineering, University of Bath, Claverton Down, Bath, UK

Self-induced flow occurs when a tube, with one end open and the other sealed, is rotated about its axis: fluid flows along the axis towards the sealed end and returns in an annular layer on the cylindrical wall. Numerical solutions of the Navier–Stokes and energy equations have been obtained for laminar flow, and the Reynolds analogy has been used to provide theoretical correlations for the average Nusselt numbers on the end wall of the tube. Heat transfer measurements have been made in a rotating-tube rig, and the measured Nusselt numbers are, in the main, in good agreement with the computed values.

Keywords: self-induced flow; rotating tube; heat transfer; rotating flow

1. Introduction

Self-induced flow occurs where a tube, with one end open and the other sealed, is rotated about its axis: fluid flows along the axis towards the sealed end and returns in an annular layer on the cylindrical surface.

A chance discovery was made by Rolls Royce engineers during anti-icing tests on the nose bullet of an aeroengine. The rotating nose bullet, which was attached to the compressor shaft at the front of the engine by an anti-icing tube, was kept free of ice by blowing hot air along the hollow shaft, as illustrated in Figure 1. The hot air, extracted from the enclosed space next to the last stage of the turbine, flowed along the compressor shaft, passed through the anti-icing tube, and impinged on the back of the nose bullet. Unfortunately, after being exhausted through vents in the nose bullet, the hot air was ingested into the compressor intake, causing a loss of performance.

The engineers overcame the problem of ingestion by blocking the outlet holes in the anti-icing tube. This, they believed, would reduce the effectiveness of the anti-icing system, but they hoped that the engine would still be able to operate for short periods under conditions where icing was liable to occur. Although there was no longer a superimposed flow of air through the compressor shaft, the anti-icing was surprisingly effective. The "hot-poker effect," as it was christened, was attributed to thermosyphon effects, and was patented by Rolls Royce in (1979).

The discovery that this effect was caused by self-induced flow, rather than by a thermosyphon phenomenon, was made by Owen and Pincombe (1981). They conducted flow visualization in a circular glass rotating tube and observed the passage of smoke along the axis from the open end to the sealed end and its return along the cylindrical surface, as shown schematically in Figure 2. The authors also conducted some simple heat transfer tests that, although inconclusive, supported the contention that self-induced flow was responsible for the hot-poker effect found by the Rolls Royce engineers. Owen and Pincombe used the term *long-tube* for the case where the self-induced flow did not reach the sealed end, and *short-tube* for the case where it did. The long-tube case is associated with tubes of large length-to-diameter (L/D) ratios or low rotational speeds; the short-tube case is associated with small L/D ratios or high rotational speeds.

The principle of self-induced flow can be explained in simple terms. Consider an isothermal rotating tube sealed at both ends: solid-body rotation occurs, and the resulting centripetal acceleration of the fluid is balanced by the pressure gradient;

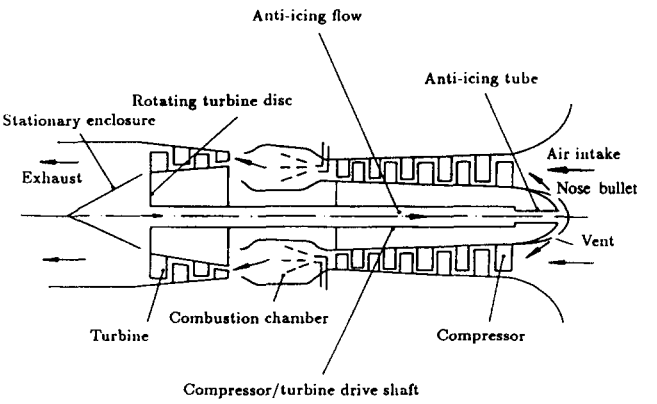

Figure 1 Schematic diagram of a gas-turbine aeroengine showing anti-icing system for the nose bullet

Address reprint requests to Professor Owen at the School of Mechanical Engineering, University of Bath, Claverton Down, Bath BA2 7AY, UK.

Received 28 November 1991; accepted 27 April 1992

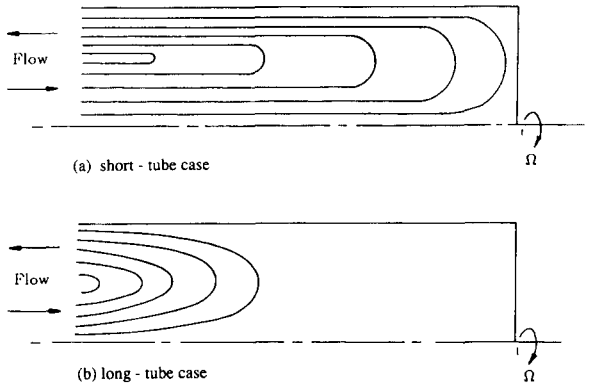

Figure 2 Schematic diagram showing self-induced flow in a rotating tube

at the ends of the tube, the radial pressure gradient is reacted by forces on the end walls. However, if an end wall is removed, the pressure gradient can no longer be balanced: the high-pressure fluid near the outside of the tube flows out of the open end to be replaced by an axial inflow along the axis. While this flow may be modified by buoyancy forces, it is not caused by them.

Ivey (1988) extended the above, preliminary, investigation of self-induced flow. He used laser-Doppler anemometry (LDA) to make measurements of the velocity inside tubes of various L/D ratios and tubes with sudden changes of section, or "stepped tubes," such as occur in the compressor shafts of aeroengines. For the short-tube case, the flow rate decreased with axial distance from the inlet, and air was recirculated continuously from the core to the annular layer. The flow and heat transfer at the sealed end were similar to the "free-disc" case (that is, an infinite disc rotating in a quiescent fluid); however, the flow rate at the open end was much larger than the free-disc entrainment rate. Ivey also showed that the self-induced flow was sensitive to the level of swirl in the air outside the open end. For the "stepped-tube" case, he found that the flow at the sealed end of the small-diameter tube was controlled mainly by the rotational speed and L/D ratio of this tube and not by the geometry of the larger tube.

Gilham (1990) conducted a theoretical investigation and obtained numerical solutions of the Navier–Stokes and energy equations for a constant-diameter tube. His computed velocity profiles were, in the main, in good agreement with Ivey's measurements and confirmed that the flow was indeed laminar, even at conditions representative of those in aeroengines. Gilham also obtained solutions of the so-called "linear equations", in which the nonlinear inertia terms in the Navier–Stokes equations are negligibly small compared with the Coriolis terms.

The two important nondimensional parameters in this problem are the length-to-radius ratio, G, and the Ekman number, E, where

$$G = \frac{l}{a} \tag{1}$$

and

$$E = \frac{\nu}{\Omega a^2} \tag{2}$$

Notation

a	Internal radius of tube
b	Outer radius of disc at open end of tube
C_m	Moment coefficient, $M/\frac{1}{2}\rho\Omega^2 a^5$
C_p	Specific heat at constant pressure
C_w	Nondimensional mass flow rate, $m/\mu a$
E	Ekman number, $\nu/\Omega a^2$ $(= \mathrm{Re}_\phi^{-1})$
E^*	Modified Ekman number, GE
Ec	Eckert number, $\Omega^2 a^2/C_p\Delta T$
G	Aspect ratio, l/a
H	Total enthalpy, $C_pT + \frac{1}{2}(u^2 + v^2 + w^2)$
k	Thermal conductivity
l	Length of tube
m	Mass flow rate
M	Frictional moment on wall
Nu	Local Nusselt number, $qr/k(T_\infty - T_o)$
Nu*	Modified local Nusselt number, $qr/k(T_{o,ad} - T_o)$
Nu_{av}	Average Nusselt number, $q_{av}a/k(T_\infty - T_o)_{av}$
Nu^*_{av}	Modified average Nusselt number, $q_{av}a/k(T_{o,ad} - T_o)_{av}$
p	Static pressure
Pr	Prandtl number, $\mu C_p/k$
q	Local heat flux from fluid to wall
r	Radial coordinate
R	Recovery factor
RMS_Φ	Root-mean-square residual
Re_ϕ	Rotational Reynolds number, $\Omega a^2/\nu = E^{-1}$
T	Temperature
u	Radial component of velocity
v	Tangential component of velocity relative to a stationary frame
w	Axial component of velocity
z	Axial coordinate measured from open end of tube

Greek symbols

β	Coefficient of volumetric expansion
Γ	Diffusion coefficient
δ	Thickness of boundary layer
ΔT	Magnitude of temperature difference between fluid and wall, $\lvert T_\infty - T_o \rvert$
θ	Nondimensional temperature, $(T - T_o)/(T_\infty - T_o)$
μ	Dynamic viscosity
ν	Kinematic viscosity, μ/ρ
ρ	Density
τ_ϕ	Tangential component of shear stress
Ω	Angular speed of tube
$\mathfrak{R}$	Gas constant

Subscripts

a	Value at cylindrical wall, $r = a$
ad	Adiabatic value
atm	Atmospheric value
av	Radially-weighted average value
fd	Free-disc value
flux	Pertaining to fluxmeter
l	Value at end wall, $z = l$
o	Value at cylindrical or end wall
r, ϕ, z	Radial, tangential, axial directions
Φ	Pertaining to dependent variable
∞	Pertaining to fluid at inlet to system

Gilham's linear solutions showed that, for large values of G and small values of E, the solutions could be characterized by a single nondimensional parameter, E^*, a modified Ekman number defined as

$$E^* = GE \tag{3}$$

For $E^* > 0.2$, the long-tube case, recirculation is confined to the open end of the tube, and the axial component of velocity decays exponentially along the tube. For $E^* < 0.2$, the short-tube case, recirculation occurs throughout the tube, and an Ekman layer (Ekman 1905) forms on the center of the end wall. For $E^* < 0.0025$, there is an inviscid central core with Stewartson-type layers (Stewartson 1957) on the cylindrical surface and an Ekman layer over most of the end wall. These regimes are similar to those found by Brouwers (1976) for the linear equations applied to a rotating tube with differentially rotating porous end walls. For the anti-icing tube mentioned above, $G \approx 30$ and $E^* \approx 0.002$.

The self-induced flow in constant-diameter and stepped tubes has been described in detail by Gilham *et al.* (1991, 1992a). The work described below concentrates mainly on the related heat transfer to the end wall; heat transfer to the cylindrical wall of the tube, and the application to the design of anti-icing systems, is reported by Gilham *et al.* (1992b).

The numerical method is outlined in Section 2, the apparatus is described in Section 3, and the heat transfer results are discussed in Section 4.

2. Numerical method

2.1. Equations of motion and energy equation

For a Newtonian fluid, the equations governing the conservation of momentum, mass, and energy are given by the Navier–Stokes, continuity and energy equations. In stationary cylindrical-polar coordinates (r, ϕ, z), assuming the flow to be steady, axisymmetric, and laminar, the equations are (see Bird, Stewart, and Lightfoot 1960):

$$\frac{1}{r}\frac{\partial}{\partial r}(\rho r u^2) + \frac{\partial}{\partial z}(\rho w u) = -\frac{\partial p}{\partial r} + \frac{\rho v^2}{r} + \frac{1}{r}\frac{\partial}{\partial r}\left(\frac{4}{3}\mu r\frac{\partial u}{\partial r}\right) + \frac{\partial}{\partial z}\left(\mu\frac{\partial u}{\partial z}\right) - \frac{2}{3}\frac{u}{r}\frac{\partial \mu}{\partial r} - \frac{4}{3}\mu\frac{u}{r^2} - \frac{2}{3}\frac{\partial}{\partial r}\left(\mu\frac{\partial w}{\partial z}\right) + \frac{\partial}{\partial z}\left(\mu\frac{\partial w}{\partial r}\right) \tag{4}$$

$$\frac{1}{r}\frac{\partial}{\partial r}(\rho r u v) + \frac{\partial}{\partial z}(\rho w v) = -\frac{\rho u v}{r} + \frac{1}{r}\frac{\partial}{\partial r}\left(\mu r\frac{\partial v}{\partial r}\right) + \frac{\partial}{\partial z}\left(\mu\frac{\partial v}{\partial z}\right) - \frac{\mu v}{r^2} - \frac{v}{r}\frac{\partial \mu}{\partial r} \tag{5}$$

$$\frac{1}{r}\frac{\partial}{\partial r}(\rho r u w) + \frac{\partial}{\partial z}(\rho w^2) = -\frac{\partial p}{\partial z} + \frac{1}{r}\frac{\partial}{\partial r}\left(\mu r\frac{\partial w}{\partial r}\right) + \frac{\partial}{\partial z}\left(\frac{4}{3}\mu\frac{\partial w}{\partial z}\right) - \frac{2}{3}\frac{\partial}{\partial z}\left(\mu\frac{1}{r}\frac{\partial}{\partial r}(ru)\right) + \frac{1}{r}\frac{\partial}{\partial r}\left(\mu r\frac{\partial u}{\partial z}\right) \tag{6}$$

$$\frac{1}{r}\frac{\partial}{\partial r}(\rho r u) + \frac{\partial}{\partial z}(\rho w) = 0 \tag{7}$$

$$\frac{1}{r}\frac{\partial}{\partial r}(\rho r u H) + \frac{\partial}{\partial z}(\rho w H) = \frac{1}{r}\frac{\partial}{\partial r}\left(\frac{k}{C_p} r\frac{\partial H}{\partial r}\right) + \frac{\partial}{\partial z}\left(\frac{k}{C_p}\frac{\partial H}{\partial z}\right) + S_H \tag{8}$$

where

$$S_H = \frac{1}{r}\frac{\partial}{\partial r}\left[\left(\mu - \frac{k}{C_p}\right) r\frac{\partial}{\partial r}\left(\frac{u^2+v^2+w^2}{2}\right)\right] + \frac{\partial}{\partial z}\left[\left(\mu - \frac{k}{C_p}\right)\frac{\partial}{\partial z}\left(\frac{u^2+v^2+w^2}{2}\right)\right] + \frac{1}{r}\frac{\partial}{\partial r}\left[\mu r\left(\frac{1}{3}u\frac{\partial u}{\partial r} - \frac{2}{3}\frac{u^2}{r} - \frac{2}{3}u\frac{\partial w}{\partial z} - \frac{v^2}{r} + w\frac{\partial u}{\partial z}\right)\right] + \frac{\partial}{\partial z}\left[\mu\left(u\frac{\partial w}{\partial r} + \frac{1}{3}w\frac{\partial w}{\partial r} - \frac{2}{3}\frac{w}{r}\frac{\partial}{\partial r}(ru)\right)\right] \tag{9}$$

Here p, ρ, and μ denote pressure, density, and dynamic viscosity, respectively, and (u, v, w) are the velocity components in the (r, ϕ, z) directions. The stagnation enthalpy is denoted by H $(H = C_p T + \frac{1}{2}(u^2 + v^2 + w^2))$, C_p is the specific heat capacity, which is assumed constant in the derivation of Equation 8, and k is the thermal conductivity.

Solutions are presented below for both compressible and incompressible flow. For compressible flow, it was assumed that the density ρ was given by the equation of state for a perfect gas:

$$\rho = \frac{p}{\Re T} \tag{10}$$

Here $\Re$ denotes the gas constant, which for air is 287 J/kgK, and T the temperature in Kelvin. The dynamic viscosity, μ [kg/ms], was assumed to vary according to Sutherland's law, which for air is

$$\mu = \frac{1.46 \times 10^{-6} T^{3/2}}{(110 + T)} \tag{11}$$

The thermal conductivity, k [W/mK], was evaluated according to

$$k = \frac{\mu C_p}{\mathrm{Pr}} \tag{12}$$

where Pr is the Prandtl number, which was assumed constant and equal to 0.71, and C_p was taken as 1.00 kJ/kgK.

For incompressible flow, the density, viscosity and conductivity were assumed to be constant, which allowed Equations 4 to 9 to be simplified.

2.2. Boundary conditions

2.2.1. Open end of tube. It is difficult to specify boundary conditions at the open end of the tube ($z = 0$, $r < a$), since there is strong recirculation here. In his experiments, Ivey (1988) used a stationary enclosure around the open end, but Gilham (1990) found that the problem of computing the flow inside the enclosure could be as difficult as that of computing the flow in the rotating tube.

As shown in Figure 1, in an aeroengine there is a rotating disc attached to the compressor shaft near the open end. Ivey found that the attachment of a rotating disc to the open end of the rotating tube had only a small effect on the velocity measured near the sealed end. The inclusion of a rotating disc in the mathematical model of the rotating tube has the advantage of simplifying the specification of the boundary conditions near the open end. By placing the boundaries on

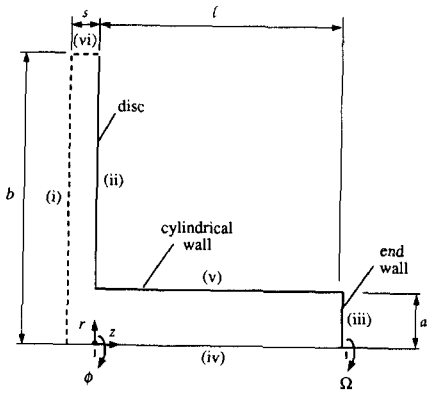

Figure 3 Domain of integration for the rotating tube and disc (Roman numerals refer to boundaries)

the left-hand side of the disc (see Figure 3), the fluid enters the system axially through boundary (i) and leaves radially through boundary (vi).

The problem can be further simplified by applying the von Karman (1921) equations for the "free disc" to an annular disc, of inner radius a and outer radius b, attached to the open end of the rotating tube (see Gilham et al. 1991a). Boundary (i) shown in Figure 3 is assumed to be far enough away from the disc for the conditions at infinity to apply at $z = -s$, so that

$$u = 0, \quad v = 0, \quad p = p_{atm}, \quad \text{at } z = -s \tag{13}$$

where p_{atm} is the atmospheric pressure. The radius of the disc is assumed to be large enough so that the von Karman similarity solutions are applicable, and

$$\frac{\partial}{\partial r}\left(\frac{u}{r}\right) = 0, \quad \frac{\partial}{\partial r}\left(\frac{v}{r}\right) = 0, \quad \frac{\partial w}{\partial r} = 0, \quad \frac{\partial p}{\partial r} = 0 \tag{14}$$

Equations 13 and 14 ensure that, as for the free-disc case, fluid enters the system axially through boundary (i) and leaves radially through boundary (vi).

The radius of the disc was set at $b = 5a$ and, for most cases, $s = a$, which ensured that $\delta \ll s$, where $\delta = 5.5\sqrt{\nu/\Omega}$ is the approximate thickness of the boundary layer on the free disc. For the case of a solid disc, Gilham (1990) found that a value of $s = 4\delta$ was sufficient to ensure that the computed velocity profiles were in good agreement with the free-disc solutions of Rogers (see Owen and Rogers 1989).

2.2.2. Conditions for the six boundaries. All solid surfaces were assumed to be at the same temperature, $T = T_o$, and no-slip conditions were applied at these surfaces. At the inlet to the system, the fluid temperature T_∞ was taken to be 20°C, and the free-disc conditions discussed above were used for the velocity. The atmospheric pressure was taken to be $p_{atm} = 1$ bar, and all nondimensional parameters were based on properties calculated at $T = T_\infty$ and $p = p_{atm}$. For the tube axis, $r = 0$, symmetry conditions were assumed for w and T.

The conditions for the six boundaries shown in Figure 3 are given below.

(i) $z = -s, 0 \leqslant r \leqslant b: u = 0, v = 0, p = p_{atm}, T = T_\infty$

(ii) $z = 0, a \leqslant r \leqslant b: u = 0, v = \Omega r, w = 0, T = T_o$

(iii) $z = l, 0 \leqslant r \leqslant a: u = 0, v = \Omega r, w = 0, T = T_o$

(iv) $r = 0, -s \leqslant z \leqslant l: u = 0, v = 0, \dfrac{\partial w}{\partial r} = 0, \dfrac{\partial T}{\partial r} = 0$

(v) $r = a, 0 \leqslant z \leqslant l: u = 0, v = \Omega a, w = 0, T = T_o$

(vi) $r = b, -s \leqslant z \leqslant o: \dfrac{\partial}{\partial r}\left(\dfrac{u}{r}\right) = 0, \dfrac{\partial}{\partial r}\left(\dfrac{v}{r}\right) = 0, \dfrac{\partial w}{\partial r} = 0, \dfrac{\partial T}{\partial r} = 0$ (15)

2.3. Solutions of finite-difference equations

The finite-difference equations were obtained by integrating the momentum and energy equations over a control volume formed in a rectangular, nonuniform, staggered grid system, as recommended by Patankar (1980) and Patankar and Spalding (1972). The nonuniform grid was generated using a geometric progression, with a maximum grid-expansion factor of 1.3.

Equations 4, 5, 6, and 8 can be expressed in the common form:

$$\frac{1}{r}\frac{\partial}{\partial r}(\rho r u \Phi) + \frac{\partial}{\partial z}(\rho w \Phi) = \frac{1}{r}\frac{\partial}{\partial r}\left(r\Gamma_{\Phi,r}\frac{\partial \Phi}{\partial r}\right) + \frac{\partial}{\partial z}\left(\Gamma_{\Phi,z}\frac{\partial \Phi}{\partial z}\right) + S_\Phi \tag{16}$$

where Φ represents the dependent variables u, v, w, and H, $\Gamma_{\Phi,r}$, and $\Gamma_{\Phi,z}$ are diffusion coefficients and S_Φ is a source term. Integration of Equation 16 over a control volume (see Patankar 1980) leads to the finite-difference equation:

$$A_{p,\Phi}\Phi_p = \Sigma_{nb} A_{nb,\Phi}\Phi_{nb} + S_{1,\Phi} + S_{2,\Phi}\Phi_p \tag{17}$$

Here Σ_{nb} represents the summation of the coefficients over four neighboring nodes, Φ_{nb} are the values of Φ at these nodes, $S_{1,\Phi}$ and $S_{2,\Phi}$ are the coefficients of the linearized source term, and $A_{p,\Phi}$ and $A_{nb,\Phi}$ are coefficients resulting from the integration. Further details are given by Gilham (1990).

The continuity equation, Equation 7, was used to devise a pressure-correction equation, as described by van Doormaal and Raithby (1984). This equation, which has the same form as Equation 17, has the dual role of determining the pressure and satisfying continuity.

Boundary conditions were applied at the boundary nodes, and derivatives were calculated by second-order backward differences or central differences. When the pressure at a boundary was specified, the pressure-correction was set to zero. This implied that continuity was satisfied for that cell, which allowed the continuity equation to be written in a finite-difference form that could be solved to evaluate the velocity components. Starting conditions were obtained by setting all variables to zero.

The resulting finite-difference equations were solved using the nonlinear multigrid algorithm of Vaughan et al. (1989), and further details are given by Gilham (1990). Underrelaxation was implemented implicitly, via the coefficients, for the momentum and energy equations and explicitly for the pressure; underrelaxation factors were in the range 0.3 to 0.8. Numerical instabilities resulting from the strong coupling between the radial and tangential momentum equations were reduced by the method suggested by Gosman et al. (1976).

Convergence was tested by means of a root-mean-square residual, RMS_Φ, defined as

$$RMS_\Phi = \sum_{ij}\sqrt{(\Phi^n - \Phi^{n-1})^2}\Big/\sum_{ij}(\Phi^n)^2$$

where Φ^n, Φ^{n-1} are the current and previous iterative values of the dependent variable on the finest mesh, and $\sum_{ij}$ is the summation over all grid nodes. Convergence was based on the criterion that RMS_Φ was less than a specified value, and overall balances in conserved quantities were also used to ensure convergence; for momentum and continuity, $RMS_\Phi < 10^{-5}$,

and for energy, $RMS_\Phi < 10^{-6}$. As discussed by Gilham (1990), computed values of moment coefficients and Nusselt numbers were in good agreement with solutions of the linear equations; although only limited grid-dependency tests were conducted, the results presented in this paper should be accurate enough for all practical purposes.

Computations were conducted for $5 \leqslant G \leqslant 40$ and $5 \times 10^{-5} \leqslant E \leqslant 0.04$, and the number of nodes used depended on G and E. For example, for $G = 10$ and $E = 2 \times 10^{-3}$, a total of 128 axial and 65 radial nodes were used in the tube, and 65 axial and 97 radial nodes were used in the region outside the open end. For incompressible flow, the multigrid method required 89 iterations for solution of the momentum equations, which took 672 minutes of CPU time on a VAX 8530 computer; solution of the energy equation required 29 iterations, which took 97 CPU minutes. More time was required for the compressible cases, since the momentum and energy equation could not be uncoupled; as a consequence, comparatively few computations were made for compressible flow.

3. Experimental apparatus

3.1. Heat transfer rig

The heat transfer rig is shown in Figure 4. The rotating tube, which was made from stainless steel, was 531 mm long and 37 mm in diameter ($G \approx 28.8$). One end of the tube was sealed by an end cap, which housed a heat-fluxmeter, and the other end opened into a large, stationary open-end enclosure. The temperature of the air inside the enclosure was varied by means of an electric heater.

The rotating tube assembly was mounted in ball bearings and was driven, via a toothed belt and pulley system, by a variable-speed electric motor. The rotational speed, which could be varied up to 5200 rev/min, was measured to an accuracy of 1 percent by a stationary transducer and a rotating inductive disc attached to the tube.

The cylindrical surface of the rotating tube was surrounded by an annulus, with a radial height of 10 mm, and the temperature of the cylindrical surface was controlled by varying the temperature of the air blown through the annulus. A bearing sleeve, passing through the inner race of the ball bearings, formed part of the outer wall of the annulus, and the rotating tube was driven by three radial supports attached to each sleeve. The remainder of the outer wall of the annulus was formed by stationary tubes, on either side of the bearing sleeves. Air entered and left the annulus through ducts attached to the stationary tubes, and seals were used to minimize leakage between the rotating and stationary components.

3.2. Thermal instrumentation

Eight copper–constantan thermocouples were used to measure the temperature of the outer surface of the tube, and a further eight were used to measure the air temperature on the axis ($r = 0$). The signals from the rotating thermocouples, together with those from the fluxmeter described below, were brought out through a silver slip-ring assembly attached by drive-tubes to the sealed end of the tube, as shown in Figure 4. The air temperatures in the stationary enclosure at the open end, and in the ducts entering and leaving the annulus, were measured by stationary thermocouples. The thermocouple voltages were measured by a computer-controlled Solartron data-logger, the digital voltmeter of which had a resolution of 1 μV (approximately 0.02°C for copper–constantan thermocouples). The maximum errors in the measured temperatures of the rotating and stationary thermocouples were determined as 0.5°C and 0.2°C, respectively.

The average heat flux through the sealed end of the tube was measured by means of a purpose-built fluxmeter (see Figure 5), which was designed to promote an axial flow of heat from a copper disc to a copper plug, the latter being cooled by convection to the surrounding atmosphere. The fluxmeter was of composite construction comprising a thermal insulator ($k \approx 0.2$ W/mK) of 1-mm thickness and 24-mm diameter sandwiched between the copper disc of 0.5-mm thickness and the copper plug of 6-mm thickness, with copper–constantan thermocouples embedded in the faces of the disc and plug on either side of the insulator. The dimensions of the copper disc were chosen to reduce radial heat transfer and to provide a uniform temperature on the adjacent insulator. The outer flat surface of the copper disc, which was exposed to the self-induced flow in the rotating tube, was gold plated (emissivity ≈ 0.05) to reduce radiation between the disc and the tube surface. The fluxmeter assembly was surrounded with a cylindrical layer of

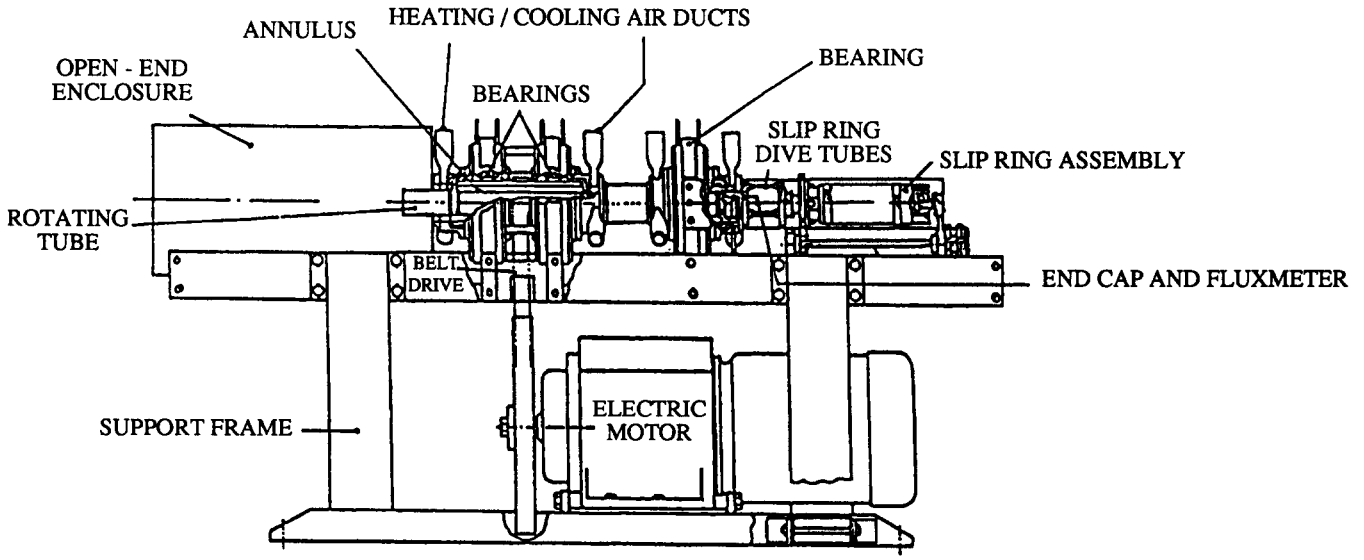

Figure 4 Heat transfer rig

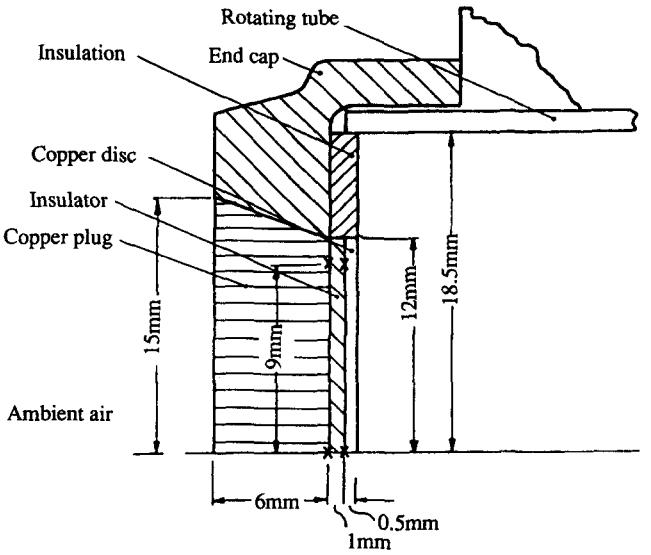

Figure 5 Details of fluxmeter. ×, Location of thermocouples

thermal insulation, $k \approx 0.04$ W/mK, to reduce radial conduction to the tube, and the assembly was clamped to the end of the tube by means of an end cap.

The fluxmeter was calibrated statically, in a purpose-built calibration rig, by heating the copper disc with a thin-foil electric heater and cooling the copper plug with an air jet. The uncertainty in the effective heat transfer coefficient measured during the calibration was ±3 percent, and the flux values were consistent with the manufacturers' quoted thermal conductivity for the materials used. (The uncertainties in the calibration and in the measured temperature differences were used to estimate the experimental uncertainties in the Nusselt numbers shown in Figures 9 and 10.)

Full details of the fluxmeter, instrumentation, calibration, and experimental uncertainties are given by Ivey (1988).

4. Heat transfer in the rotating tube

4.1. Computed isotherms

Figure 6 shows the computed isotherms for incompressible flow for $G = 40$ and $E^* = 2 \times 10^{-2}$, 2×10^{-3}, and 2×10^{-4}. The nondimensional temperature, θ, is defined as

$$\theta = \frac{T - T_o}{T_\infty - T_o} \tag{18}$$

where the temperature of the air at inlet to the tube is $T_\infty = 20°C$ and the wall temperature is $T_o = 0°C$. This corresponds to the so-called "heating case" where the air is hotter than the tube ($T_\infty > T_o$). Isotherms for the "cooling case" ($T_\infty < T_o$), and for other values of G, are similar to those shown in Figure 6.

Owing to the scale chosen for the figure, the steep gradients cannot be seen at the sealed end, where $\theta = 0$. This is particularly true for $E^* = 2 \times 10^{-3}$ and 2×10^{-4}, where the Ekman layer (the thickness of which is proportional to $E^{1/2}$) is very thin.

In all cases, heat flows from the open end towards the sealed end. For $E^* = 2 \times 10^{-2}$, where the self-induced flow is very weak, the heat transfer is mainly by conduction. For the other cases, the thermal boundary layer on the cylindrical surface becomes thinner as E^* is reduced; the same is true of the thermal boundary layer on the end wall, but, as stated above, this cannot be seen owing to the scale of the figure. For $E^* = 2 \times 10^{-4}$, the temperature of the core of fluid near the axis is virtually isothermal and equal to the temperature of the air outside the tube: the isotherms shown are inside the velocity boundary layer on the cylindrical surface.

4.2. Computed Nusselt numbers for the sealed end

Gilham et al. (1991a) showed that the flow near the end wall of the rotating tube was similar to that of the free disc. For an isothermal ($T = T_o$) free disc rotating in air (Pr = 0.71), the exact solution of the incompressible energy equation with negligible viscous dissipation (see Owen and Rogers 1989) gives

$$E^{1/2}\,\mathrm{Nu}_l = 0.326\left(\frac{r}{a}\right) \tag{19}$$

where Nu_l, the Nusselt number for the end wall, is defined as

$$\mathrm{Nu}_l = \frac{q_l r}{k(T_\infty - T_o)} \tag{20}$$

and

$$q_l = -k\left(\frac{\partial T}{\partial z}\right)_{z=l} \tag{21}$$

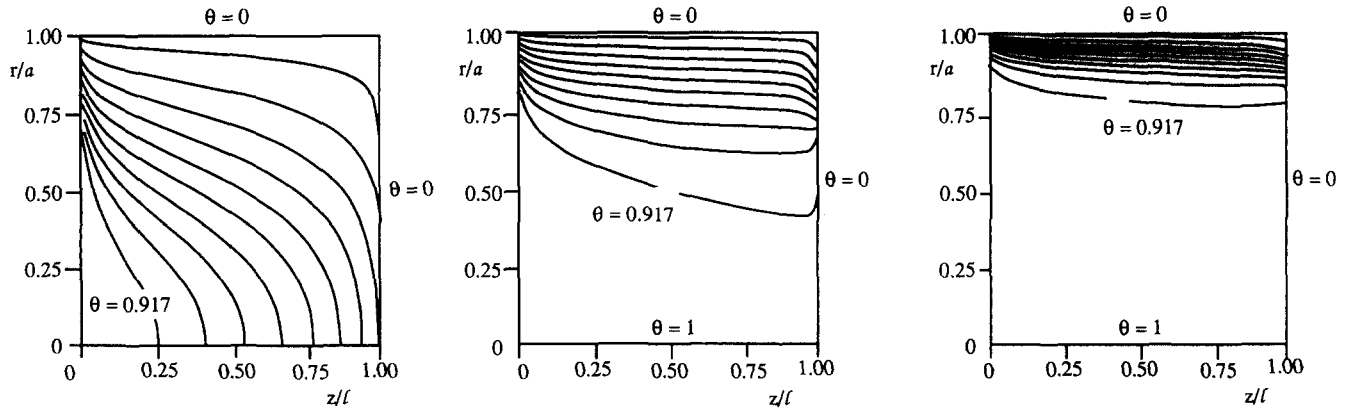

(a) $E^* = 2\text{x}10^{-2}$, $Ec = 1.15 \times 10^{-4}$ (b) $E^* = 2\text{x}10^{-3}$, $Ec = 1.15 \times 10^{-2}$ (c) $E^* = 2\text{x}10^{-4}$, $Ec = 1.15$

Figure 6 Computed isotherms for heating case: $G = 40$

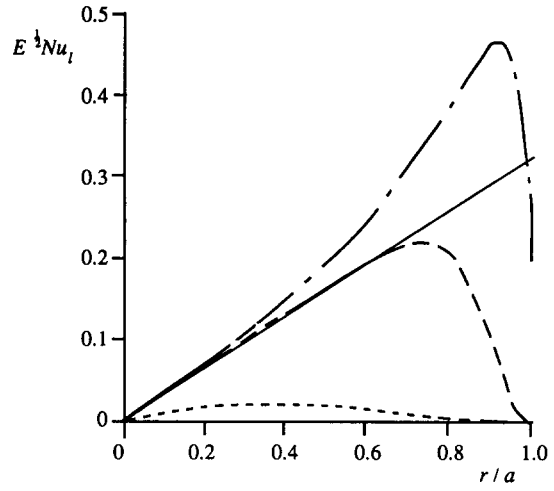

Figure 7 Computed radial variation of Nusselt numbers at sealed end for heating case: $G = 40$. ---, $E^* = 2 \times 10^{-2}$; Ec = 1.15×10^{-4}; ——, $E^* = 2 \times 10^{-3}$; Ec = 1.15×10^{-2}; — · —, $E^* = 2 \times 10^{-4}$; Ec = 1.15; ———, Equation 19

Figure 7 shows the computed variation of $E^{1/2}\,\mathrm{Nu}_l$ with r/a for the heating case with $G = 40$ and $E^* = 2 \times 10^{-2}, 2 \times 10^{-3}$, 2×10^{-4}; also shown is the free-disc result given by Equation 19. The Nusselt number increases with radius, reaches a maximum, and then decreases towards the outer edge of the end wall at $r/a = 1$. This decrease is associated with the boundary layer on the cylindrical surface, which was referred to above. For $E^* = 2 \times 10^{-2}$, the Nusselt number is small; for $E^* = 2 \times 10^{-3}$, Nu_l is close to the free-disc value for $r/a < 0.7$; for $E^* = 2 \times 10^{-4}$, Nu_l exceeds the free-disc value over most of the radius.

As E^* is reduced, two effects occur: more of the end wall is exposed to the self-induced flow, and viscous dissipation increases. Dissipation, or frictional heating, increases the transfer of heat from the fluid to the end wall. For the heating case discussed above, frictional heating can increase the Nusselt number above the free-disc value. For the cooling case, however, frictional heating reduces the Nusselt number so that it is always lower than the free-disc value.

The magnitude of the frictional heating depends on the Eckert number, Ec

$$\mathrm{Ec} = \frac{\Omega^2 a^2}{C_p \Delta T} \tag{22}$$

where $\Delta T = |T_\infty - T_o|$. For $G = 40$ and $E^* = 2 \times 10^{-2}$, 2×10^{-3} and 2×10^{-4}, Ec = 1.15×10^{-4}, 1.15×10^{-2} and 1.15, respectively.

The influence of frictional heating on the calculated Nusselt number can be reduced by the use of an adiabatic-disc temperature $T_{o,\mathrm{ad}}$ (see Owen and Rogers 1989) where

$$T_{o,\mathrm{ad}} = T_\infty + R\frac{\Omega^2 r^2}{2C_p} \tag{23}$$

and R is a recovery factor, which for air can be approximated by $R \approx \mathrm{Pr}^{1/3}$. A modified Nusselt number is then defined as

$$\mathrm{Nu}_l^* = \frac{q_l r}{k(T_{o,\mathrm{ad}} - T_o)} \tag{24}$$

and this is less sensitive than Nu_1 to the Eckert number. Although large values of Ec have been used in the computations, the effect of frictional heating is usually negligible for engine applications.

It is also instructive to apply the Reynolds analogy (see Owen and Rogers 1989) to the end wall. For the case of the free disc with a quadratic temperature distribution ($T_o - T_\infty \propto r^2$) and for a Prandtl number of unity, the Reynolds analogy can be expressed as

$$E\,\mathrm{Nu}_{l,\mathrm{av}}^* = \frac{C_{\mathrm{m},l}}{\pi} \tag{25}$$

where $\mathrm{Nu}_{l,\mathrm{av}}^*$ is the modified average Nusselt number. The moment coefficient, $C_{\mathrm{m},l}$, is defined by

$$C_{\mathrm{m},l} = \frac{M_l}{\frac{1}{2}\rho\Omega^2 a^5} \tag{26}$$

where M_1 is the frictional moment on the rotating disc. Equation 25, the Reynolds analogy, is exact only for the conditions stated above; for an isothermal disc and for Pr = 0.71, a modified Reynolds analogy is used, and the Nusselt number is given by

$$E\,\mathrm{Nu}_{l,\mathrm{av}}^* = 0.529\frac{C_{\mathrm{m},l}}{\pi} \tag{27}$$

The variation of $E^{-1/2}C_{\mathrm{m},l}$ with $E^{*1/4}$ is shown in Figure 8a. The computations were carried out for $G = 40$, but similar results (not shown here) were obtained for $5 \leqslant G \leqslant 40$. The numerical results can be correlated for $2 \times 10^{-4} < E^* < 2.6 \times 10^{-2}$ by

$$E^{-1/2}C_{\mathrm{m},l} = 2.36 - 4.89E^{*1/4} \tag{28}$$

For $E^* > 0.2$, the long-tube case, $C_{\mathrm{m},l} = 0$, and a transition is expected between $E^* = 0.026$ and 0.2. The free-disc value,

$$E^{-1/2}C_{\mathrm{m},l} = 1.94 \tag{29}$$

is also shown, and there is, presumably, a transition to this value as E^* tends to zero.

Applying the modified Reynolds analogy, Equation 27, to the correlated moment coefficient, Equation 28, gives

$$E^{1/2}\,\mathrm{Nu}_{l,\mathrm{av}}^* = 0.397 - 0.824E^{*1/4} \tag{30}$$

This equation is shown in Figure 8b together with the computed Nusselt numbers for $5 \leqslant G \leqslant 40$; the computations were carried out for the heating case, $T_\infty > T_o$ and Ec < 0.3. The scatter that occurs at the smaller values of E^* is caused more by the effect of dissipation than by the effect of G itself: for a given value of E^*, E reduces and Ec increases with G. Use of $\mathrm{Nu}_{l,\mathrm{av}}^*$ rather than $\mathrm{Nu}_{l,\mathrm{av}}$ attenuates, but does not eliminate completely, the effect of dissipation. Consequently, the difference between the computed results and Equation 30 is greater at the larger values of G. The Reynolds analogy overestimates the Nusselt number at the larger values of E^*: under these conditions, little of the end wall is exposed to the core flow, and the analogy is inappropriate. However, for $2 \times 10^{-4} < E^* < 2 \times 10^{-3}$ and Ec < 0.3, Equation 30 should be reasonably accurate. (It is worth noting that for the anti-icing tests referred to in Section 1, $G \simeq 30$, $E^* \simeq 2 \times 10^{-3}$, and $\mathrm{Ec} \ll 1$.)

4.3. Effects of buoyancy

As stated in Section 1, the "hot-poker effect" was originally thought to be related to the thermosyphon. However, self-induced flow can occur under isothermal conditions and it is not, therefore, a thermosyphon effect. Buoyancy can, of course, modify the flow and heat transfer to the end wall of

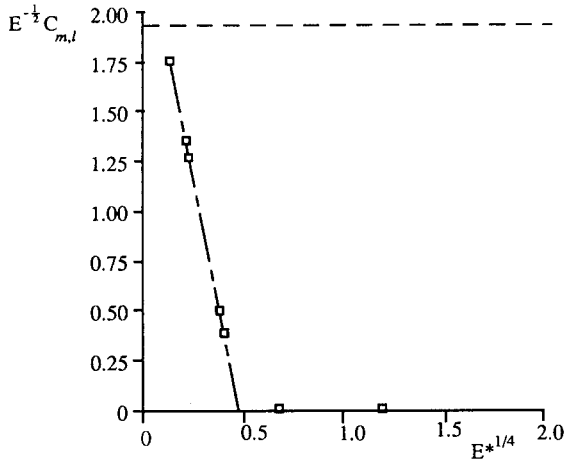

(a) Moment coefficients

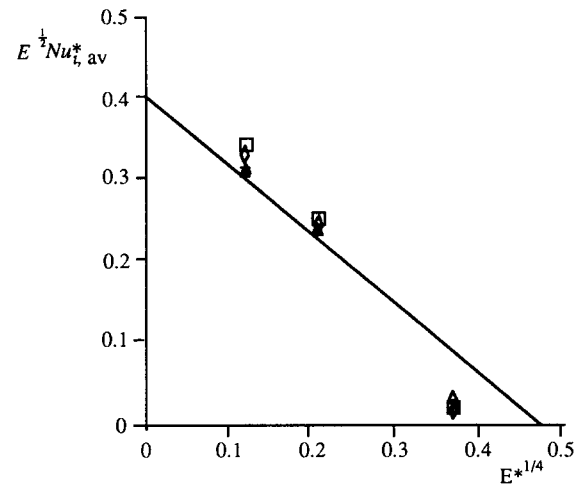

(b) Average Nusselt numbers

Figure 8 Computed moment coefficients and average Nusselt numbers at sealed end for heating case. Δ, $G = 5$; +, $G = 10$; ×, $G = 20$; ◇, $G = 30$; □, $G = 40$; ——, Equation 28; – – –, Equation 29; ———, Equation 30

the tube and, to quantify these effects, some solutions of the compressible equations 4 to 9 were obtained.

Buoyancy effects can be characterized by $\beta\Delta T$, where β is the coefficient of volumetric expansion (for air, $\beta = T_\infty^{-1}$), and $\Delta T = |T_\infty - T_o|$. (For the anti-icing tests referred to in Section 1, $\beta\Delta T \approx 0.3$.) Table 1 shows the effect of $\beta\Delta T$ on $E^{1/2}\,\mathrm{Nu}^*_{l,\mathrm{av}}$ for $G = 30$ and $E^* = 0.002$ and 0.02. It can be seen that when $\beta\Delta T$ is increased, the average Nusselt number increases in the heating case ($T_o < T_\infty$) and decreases in the cooling case ($T_o > T_\infty$). It can also be seen that the effect of $\beta\Delta T$ is relatively small for $E^* = 0.002$, but is relatively large for $E^* = 0.02$.

These effects can be explained by considering the flow near the sealed end of the tube. For large values of E^*, where the fluid near the end wall is in virtual solid-body rotation and the Nusselt numbers are small, the buoyancy forces will tend to cause the colder fluid to move radially outward and the hotter fluid to move inward. Thus, for the heating case, the buoyancy-induced flow assists the self-induced radial outflow and increases heat transfer on the end wall; for the cooling case, the effect is reversed. For small values of E^*, the fluid approaches the end wall with very little rotation, and the effects of buoyancy are weaker in both the absolute and the relative sense.

Frictional heating, like buoyancy, increases the heat transfer to the end wall for the heating case and reduces it for the cooling case. However, unlike buoyancy, frictional heating will have the greatest effect on the Nusselt numbers for small values of ΔT and for small values of E.

4.4. Comparison between theory and experiment

Ivey (1988), using the apparatus described in Section 3, made heat transfer measurements in a tube with $G = 28.8$. For most tests the temperature of the air in the stationary enclosure at the open end of the tube was heated to temperatures approximately 50°C above the ambient level of around 30°C. The hot self-induced flow caused a transfer of heat to the end wall, which was cooled externally for most of the tests by the impingement of air, at the ambient temperature, onto the outer face of the end wall. The temperature of the cylindrical surface of the tube was controlled by varying the temperature and flow rate of the air circulated through the annulus surrounding the tube.

For the so-called "adiabatic-wall tests," the temperature of the cylindrical wall was maintained approximately equal to that of the air on the axis of the tube, usually about 50°C above the ambient level. For some tests, the cylindrical wall was kept at a lower temperature than that on the axis: the cylindrical wall was kept at around 33°C, and the typical temperature on the axis decreased from around 80°C near the open end to 37°C near the end wall. It should be emphasized that both of these tests corresponded to the heating case defined above, where heat is transferred from the air to the end wall.

In the experiments, the temperature measured on the axis at $z/l = 0.892$ (the measuring point closest to the end wall) was used to determine the properties of the air; it was also used as the reference temperature, T_∞, for the Nusselt numbers. For the adiabatic-wall tests, the air temperature would not be expected to vary significantly between this location and the edge of the thermal boundary layer on the end wall.

The heat flux at the end wall was measured by the fluxmeter described in Section 3, and the Ekman number, E_{flux}, and the average Nusselt number, $\mathrm{Nu}_{l,\mathrm{flux}}$ were based on the radius of the fluxmeter a_{flux}, where $a_{\mathrm{flux}} = 0.65a$. Figure 9 shows the variation of $\mathrm{Nu}_{l,\mathrm{flux}}$ with $E_{\mathrm{flux}}^{-1/2}$ for the adiabatic-wall tests, where the temperature of the cylindrical wall and that of the air on the axis were kept at about 50°C above the ambient level. Figure 10 shows the case where the temperature of the cylindrical wall was kept at a lower temperature than that on the axis. For the latter case, the air temperature falls along the axis, and the experimentally determined Nusselt numbers are expected to be less accurate than those for the adiabatic-wall tests.

Table 1 Effect of $\beta\Delta T$ on $E^{1/2}\,\mathrm{Nu}^*_{l,\mathrm{av}}$ for $G = 30$

(a) Heating case ($T_\infty > T_o$)

	$E^* = 0.002$	$E^* = 0.02$
Incompressible	0.242	0.019
$\beta\Delta T = 0.068$	0.248	0.026
$\beta\Delta T = 0.14$	0.254	0.033

(b) Cooling case ($T_\infty < T_o$)

	$E^* = 0.002$	$E^* = 0.02$
Incompressible	0.241	0.019
$\beta\Delta T = 0.068$	0.237	0.014

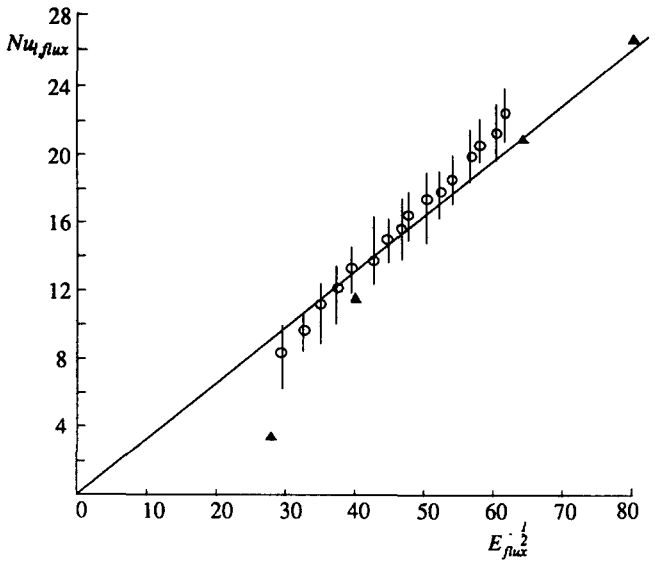

Figure 9 Comparison between measured and computed average Nusselt numbers at sealed end for $G \approx 30$: adiabatic-wall tests. ▲, computed values; ○, measured values; |, experimental uncertainty; ———, Equation 31

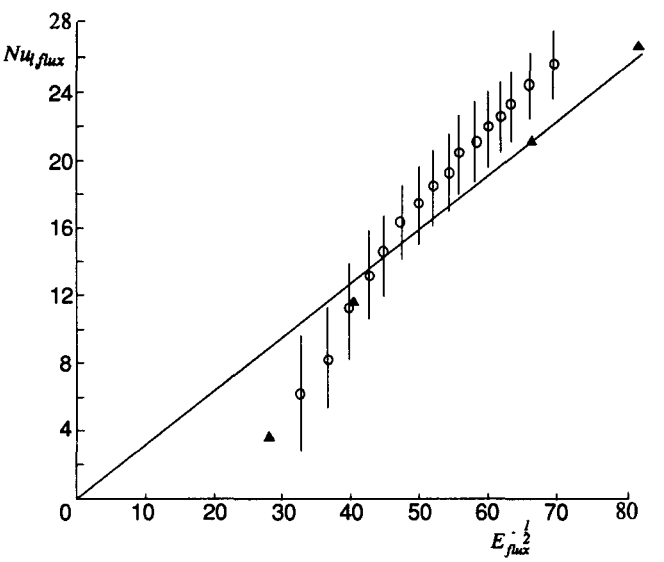

Figure 10 Comparison between measured and computed average Nusselt numbers at the sealed end for $G \approx 30$: nonadiabatic-wall tests. ▲, computed values; ○, measured values; |, experimental uncertainty; ———, Equation 31

For reference purposes, the average Nusselt number for an isothermal free disc is shown in both figures. The result, corresponding to Equation 19, is

$$\mathrm{Nu}_{l,\mathrm{flux}} = 0.326 E_{\mathrm{flux}}^{-1/2} \tag{31}$$

It should be noted that the constant of proportionality, 0.326, is independent of the radius used in the definitions of the Nusselt and Ekman numbers. (It is inappropriate to use the correlation given by Equation 30 as this only applies to the case where heat transfer occurs over the *entire* surface of the end wall.)

The computed Nusselt numbers were obtained for incompressible flow with an inlet temperature of $T_\infty = 20°C$, for the case where the surfaces of the cylindrical wall and the end wall were kept at 0°C. The average Nusselt numbers were computed by integrating the heat flux through the end wall from $r/a = 0$ to $r/a = 0.65$, corresponding to the radial extent of the fluxmeter. The computed temperature on the axis at $z/l = 0.892$, corresponding to the location used in the experiments, was taken as the reference temperature for the Nusselt numbers. For the computation, $G = 30$, compared with $G = 28.8$ for the experiments.

Figures 9 and 10 show similar effects, and the differences between the measured and computed Nusselt numbers are, in the main, within the experimental errors. Both sets of Nusselt numbers are lower than the free-disc curve for the smaller values of $E^{-1/2}$, and this is consistent with the fact that an increasing extent of the fluxmeter is exposed to the self-induced flow as the Ekman number is reduced. At the larger values of $E^{-1/2}$, the computed Nusselt numbers are close to the free-disc curve, whereas the experimental data are consistently above the curve. For the reasons stated above, the measured Nusselt numbers in Figure 10 are expected to be less accurate than those in Figure 9.

The effects of buoyancy may explain, to some extent, why the measured Nusselt numbers exceed the free-disc values. For the adiabatic-wall tests, where $\beta\Delta T \approx 0.15$, the Nusselt numbers at $E_{\mathrm{flux}}^{-1/2} = 60$ ($E^* \approx 3.4 \times 10^{-3}$) are approximately 10 percent higher than the free-disc values. (The computed results for compressible flow given in Table 1 for $E^* = 2 \times 10^{-3}$ and $\beta\Delta T = 0.14$ show an increase of around 5 percent for Nusselt numbers based on the entire surface of the end wall.) Adiabatic-wall tests conducted at a higher temperature (where $\beta\Delta T \approx 0.28$) produced experimental Nusselt numbers slightly higher than those discussed above, which supports the contention that buoyancy effects may have played some part in increasing the Nusselt numbers above the free-disc values.

5. Conclusions

Numerical solutions of the Navier–Stokes and energy equations have been obtained for the case of self-induced flow in a rotating tube with one end open and the other sealed. The heat transfer through the end wall has been measured in a tube, with a length of 531 mm and a diameter of 37 mm, rotating at speeds up to 5,200 rev/min in air.

The Reynolds analogy has been used to obtain a correlation for the computed average Nusselt numbers for the end wall, and an adiabatic-wall temperature is used to reduce the effects of viscous dissipation in the computed Nusselt numbers, which are in good agreement with the measured values. Frictional heating and buoyancy effects can increase the heat transfer to the end wall for the heating case (where the air is hotter than the wall), and can reduce it for the cooling case.

The heat transfer at the sealed end of the tube is shown to be similar to that associated with the laminar free-disc case, a finding that is consistent with earlier studies of the fluid dynamics of self-induced flow. Whilst buoyancy effects can modify the flow and heat transfer within the tube, they are unlikely to affect significantly the Nusselt numbers that occur inside the anti-icing tubes of aeroengines.

The effects of self-induced flow on the heat transfer to the cylindrical wall of a rotating tube, and the application to the design of anti-icing systems in aeroengines, is reported by Gilham *et al.* (1992b).

Acknowledgments

The work was conducted while the authors were at the University of Sussex, and we wish to thank SERC and Rolls Royce plc for funding the research program.

References

Bird, R. B., Stewart, W. D. and Lightfoot, E. N. 1960. *Transport Phenomena*. Wiley, New York

Brouwers, J. J. H. 1976. On the motion of a compressible fluid in a rotating cylinder. Doctoral thesis, University of Twente, Holland

Ekman, V. W. 1905. On the influence of the earth's rotation on ocean-currents. *Ark Mat Astra Fys*, **2**, 1–52

Gilham, S. 1990. Theoretical study of self-induced flow in a rotating tube. D.Phil. thesis, University of Sussex, England

Gilham, S., Ivey, P. C., Owen, J. M. and Pincombe, J. R. 1991. Self-induced flow in a rotating tube. *J. Fluid Mech.*, **230**, 505–524

Gilham, S., Ivey, P. C. and Owen, J. M. 1992a. Self-induced flow in a stepped rotating tube. *J. Turbomachinery*, **114**, 269–274

Gilham, S., Ivey, P. C. and Owen, J. M. 1992b. The transfer of heat by self-induced flow in a rotating tube. *ASME Int. Gas Turbine Conf.*, Cologne, Paper 92-GT-305

Gosman, A. D., Koosinlin, M. L., Lockwood, F. C. and Spalding, D. B. 1976. Transfer of heat in rotating systems. *ASME Int. Gas Turbine Conf.*, New Orleans, LA, Paper 76-GT-25

Ivey, P. C. 1988. Self-induced flow in a rotating tube. D.Phil. thesis, University of Sussex, England

Kármán, Th Von. 1921. Über laminare und turbulente Reibung. *Z. angew Math. Mech.*, **1**, 233–252

Owen, J. M. and Pincombe, J. R. 1981. Rotationally induced flow and heat transfer in circular tubes. Report 81/TFMRC/32, School of Engineering and Applied Sciences, University of Sussex, England

Owen, J. M. and Rogers, R. H. 1989. *Flow and Heat Transfer in Rotating-Disc Systems. Volume 1: Rotor-Stator Systems*. Research Studies Press, UK (Wiley Inc., USA)

Patankar, S. V. 1980. *Numerical Heat Transfer and Fluid Flow*. McGraw-Hill, New York

Patankar, S. V. and Spalding, D. B. 1972. A calculation procedure for heat and mass transfer in three-dimensional parabolic flows. *Int. J. Heat Mass Transfer*, **15**, 1787–1806

Rolls Royce Limited. 1979. Nose bullet anti-icing for gas turbine engines, UK patent GB 2,046,843B

Stewartson, K. 1957. On almost rigid rotations. *J. Fluid Mech.*, **3**, 17–26

Van Doormaal, J. P. and Raithby, G. D. 1984. Enhancement of the SIMPLE method for predicting incompressible fluid flows. *Numer. Heat Transfer*, **7**, 147–163

Vaughan, C. M., Gilham, S. and Chew, J. W. 1989. Numerical solutions of rotating disc flows using a non-linear multigrid algorithm. *Proc. 6th Int. Conf. Numer. Methods in Laminar and Turbulent Flow*, **6**, 63–73. Pineridge Press, Swansea, UK